Atomistic insights into the nanosecond long amorphization and crystallization cycle of nanoscale $Ge_2Sb_2Te_5$: An *ab initio* molecular dynamics study

Paulo S. Branicio,[1,*] Kewu Bai,[2] H. Ramanarayan,[2] David T. Wu,[2] Michael B. Sullivan,[2] and David J. Srolovitz[3]

[1]*Mork Family Department of Chemical Engineering and Materials Science, University of Southern California, Los Angeles, California 90089, USA*

[2]*Institute of High Performance Computing, Agency for Science, Technology and Research, 1 Fusionopolis Way, 16-16 Connexis 138632, Singapore*

[3]*Departments of Materials Science and Engineering & Mechanical Engineering and Applied Mechanics, University of Pennsylvania, Philadelphia, Pennsylvania 19104, USA*

(Received 7 July 2017; revised manuscript received 19 February 2018; published 6 April 2018)

The complete process of amorphization and crystallization of the phase-change material $Ge_2Sb_2Te_5$ is investigated using nanosecond *ab initio* molecular dynamics simulations. Varying the quench rate during the amorphization phase of the cycle results in the generation of a variety of structures from entirely crystallized (-0.45 K/ps) to entirely amorphized (-16 K/ps). The 1.5-ns annealing simulations indicate that the crystallization process depends strongly on both the annealing temperature and the initial amorphous structure. The presence of crystal precursors (square rings) in the amorphous matrix enhances nucleation/crystallization kinetics. The simulation data are used to construct a combined continuous-cooling-transformation (CCT) and temperature-time-transformation (TTT) diagram. The *nose* of the CCT-TTT diagram corresponds to the minimum time for the onset of homogenous crystallization and is located at 600 K and 70 ps. That corresponds to a critical cooling rate for amorphization of -4.5 K/ps. The results, in excellent agreement with experimental observations, suggest that a strategy that utilizes multiple quench rates and annealing temperatures may be used to effectively optimize the reversible switching speed and enable fast and energy-efficient phase-change memories.

DOI: 10.1103/PhysRevMaterials.2.043401

I. INTRODUCTION

Phase-change materials such as $Ge_2Sb_2Te_5$ (GST) show exceptional promise as the core component of high-performance nonvolatile phase-change memories (PCMs) which have the potential to replace flash memory and magnetic hard disk technologies in many applications [1–3]. Phase-change memories are based upon materials that exhibit fast and reversible switching between a highly resistive amorphous phase and a low resistance crystalline phase. PCMs have an outstanding set of properties which are attractive for memory applications, among them nonvolatility (important for energy efficiency), high endurance (important for device lifetime), and long data retention (important for data preservation) [4]. PCMs have other properties that make them especially promising from an engineering point of view, including random access, high scalability, multilevel programmability, and nanosecond switching times [5].

Before PCM technology is widely adopted, it is important to develop a clear, accurate, atomic-level understanding of the underlying amorphization and crystallization processes [5]. Such a mechanistic understanding is central to the rational optimization of reversible cycling time and, hence, to enhancing the ultimate performance of PCM devices [6]. The description of the fast reversible cycling of phase-change materials, in particular GST, has been elusive. Accurate first-principles calculations offer invaluable atomistic information for understanding the structure and properties of phase-change materials [7–10]. However, they provide little insight into the dynamics responsible for fast amorphization and crystallization. Recently, *ab initio* molecular dynamics (AIMD) simulations of the reversible cycling of phase-change materials, including both amorphization and (the computationally demanding) crystallization processes, have provided new insights [6,11–20].

Hegedüs and Elliot [11,12] were the first to simulate the complete phase-change switching cycle via AIMD. Following this initial work, additional AIMD simulations showed that templates can significantly enhance the speed of GeSb and Sb crystallization [13]. Lee and Elliot [14] analyzed the nucleation and initial growth of crystalline clusters in GST and concluded that fast crystallization involves the formation of medium-range ordered planar structures that lower the amorphous-crystal interfacial energy. Skelton *et al.* [21] studied the amorphization of GST using AIMD, shedding light not only on the melting and quenching process, but also on the evolution of the amorphous phase at typical device operating temperatures. Combining information from AIMD and experiments, Loke *et al.* [6] demonstrated that inducing such order can significantly reduce GST crystallization times. Kalikka *et al.* [17] showed that the introduction of a large crystalline seed in GST can reduce the crystallization time to well under a nanosecond. In line with this study, Ronneberger *et al.* [22] demonstrated that the propagation of an amorphous-crystal interface in GST is especially swift. Lee and Elliot [16] showed

*branicio@usc.edu

the important role that vacancies play in enhancing diffusion at the crystal-amorphous interface in GST [15,16]. Prasai *et al.* [18,19] showed that Ag dopants promote faster crystallization and smaller density changes during GST cycling. The AIMD simulations of Kalikka *et al.* [23] demonstrated an intriguing memory or training effect in which GST switches more rapidly following the initial amorphization-recrystallization cycle.

While these investigations provide important insights into the atomistic mechanisms of the amorphization-recrystallization cycle, strategies for optimizing the reversible cycling speed and maximizing energy efficiency remain elusive. For example, it is not clear how different quench rates affect the resulting amorphous structure. In addition, the effects of isothermal annealing temperature on the crystallization dynamics of different amorphous structures (e.g., structures produced at different quench rates) remain largely unexplored. While few experimental studies addressing these questions have been reported, the experiments of Suh *et al.* [24] suggest that the quench rate and annealing temperature may be exploited to optimize GST PCM switching rates. However, to accomplish that, more information about the thermokinetics of the amorphization and crystallization needs to be provided. The required information is typically provided in continuous-cooling-transformation (CCT) and time-temperature-transformation (TTT) diagrams, which for GST are still lacking.

In this paper, we perform a series of very long AIMD simulations (i.e., 1.5 ns) to identify the key parameters that control reversible GST switching performance. AIMD provides an accurate picture of the atomistic mechanisms responsible for both stages of the switching cycle: the complex structural relaxation occurring during the quench process and the dynamic structural changes associated with crystallization [11,13,14]. In particular, we focus on the effects of the quench rate and annealing temperature on the GST structure and the corresponding switching times.

II. COMPUTATIONAL METHODS

All AIMD simulations were performed within the density functional theory package VASP [25] using the generalized gradient approximation (GGA) with the Perdew-Burke-Ernzerhof (PBE) [26] exchange correlation energy functional. The Methfessel and Paxton method [27] was used to smear the Fermi surface and the core electrons were treated via the projector augmented-wave (PAW) method [28]. The Γ point was used to sample the Brillouin zone of the supercells. The energy cutoff was set to 175 eV for the plane-wave basis. At each AIMD time step, the electronic ground states were determined using self-consistent field iterations converged to within energy differences of less than 10^{-4} eV per cell. GST cubic supercells with 63, 108, or 207 atoms were used at a constant density of 6.11 g/cm^3. However, unless otherwise stated, the results reported are for the 108-atom supercells. A liquid GST model was generated by melting a crystal by heating to and thermalizing at 2000 K. The system was then cooled to 1073 K at a fixed rate using 50 000, 3-fs AIMD steps (i.e., -6.18 K/ps). After the liquid was thermalized at 1073 K, it was quenched to 300 K at rates of -0.45, -2, -5, and -16 K/ps. The resulting amorphous materials were then characterized to determine the effects of quench rate on the resulting atomic structure. Constant temperature annealing was performed by kinetic energy rescaling every 100 AIMD steps. All quenching and annealing simulations were performed at a constant volume. In this paper, we use the number of square rings to monitor the evolution of the structure following previous works which have used it successfully in studies of GST, given that its ring statistics is very peculiar and contrasts well between the amorphous and crystal phases [6,11,29]. Recently, a new general method for identifying nucleation and growth based on order parameters and symmetry functions has been proposed and demonstrated for the crystallization of GeTe [30].

III. RESULTS AND DISCUSSIONS

Examples of the amorphous structures generated by quenching the equilibrated 1073-K liquid GST to room temperature at different rates are shown in Fig. 1, including both the evolution of the system energy and the ring topology. The total energy decreases monotonically with time during each constant quench rate simulation [Fig. 1(a)]. The atomic structures of the GST produced by quenching at -0.45, -2, -5, and -16 K/ps are shown in Figs. 1(c)–1(f). Heat was removed from the system at 0.2, 0.9, 1.9, and 6.6 meV/ps per atom (on average) to achieve these quench rates. At early times, the nearly constant slopes shown in Fig. 1(a), $(dU/dT) = (dU/dt)/(dT/dt)$ are simply related to the heat capacity of the system C_v. Part of the change in energy during cooling is also attributable to changes in structure. The energy of the system in its crystal state is lower than that in its amorphous state; the relatively abrupt decrease in energy seen at the lowest quench rate [-0.45 K/ps; the red curve in Fig. 1(a)] at $T \sim 600$ K is indicative of crystallization. This is confirmed by an examination of the atomic structure in Fig. 1(c) and through a consideration of the bond ring statistics. Figure 1(b) shows that the number of square (4-bond) rings in the atomic structure increases abruptly around 900 K. The square ring statistics is based on the enumeration of the shortest path rings [31–34] in the bond topology constructed with a bond cutoff radius of 3.5 Å. Nonsquare rings in the atomic structure of Fig. 1(c) are the result of defects, and the number of square rings can be taken as a surrogate for crystal perfection. Note that each data point in Fig. 1(b) is averaged over a 5-ps time window to reduce fluctuations.

No abrupt drops in the energy during the higher rate quenches [Fig. 1(a)] are observed, suggesting that crystallization does not occur in these systems. This is confirmed by an examination of the atomic structures of the system at the higher rates (-5 and -16 K/ps)—see Figs. 1(e) and 1(f). However, an examination of the atomic structure following the -2 K/ps quench [Fig. 1(c)] shows the presence of a crystal nucleus within the amorphous structure. These results are confirmed by the shortest path ring statistics [Fig. 1(b)], where the two structures formed at the highest rates [Figs. 1(e) and 1(f)] show similar, low, square ring densities, but the structure formed at a -2 K/ps quench rate exhibits a square ring density that is comparable to that in the fully crystallized case [Fig. 1(c)]. Square rings are arguably crystallization precursors [11,21]. Although amorphous, the structure quenched at -5 K/ps [Fig. 1(e)]

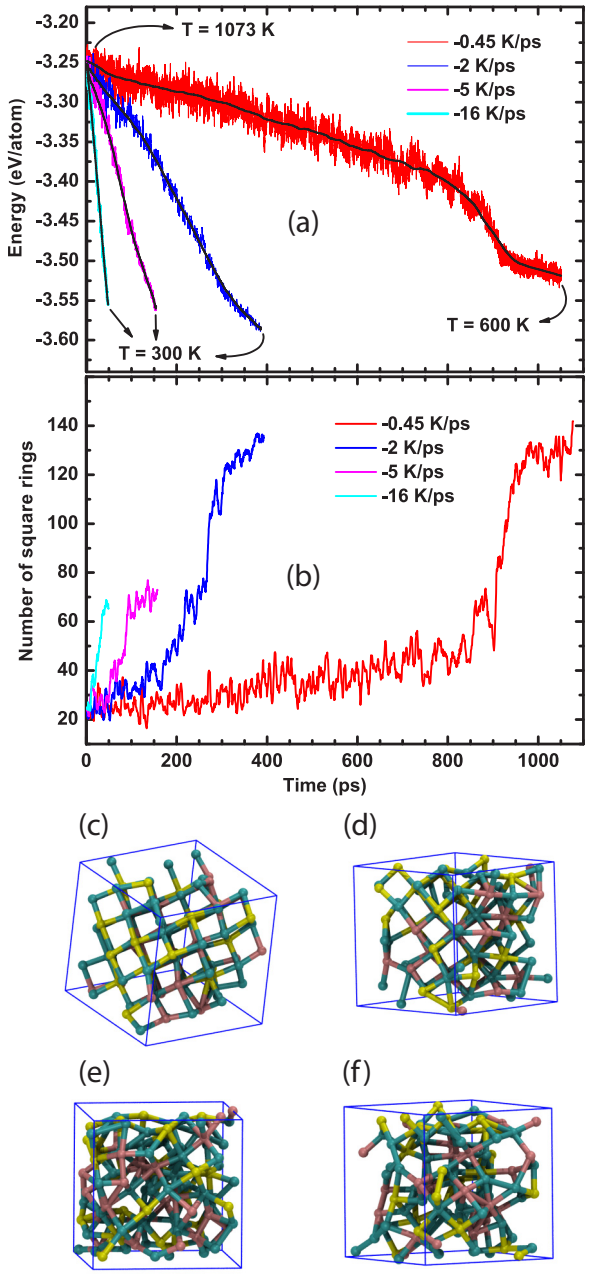

FIG. 1. $Ge_2Sb_2Te_5$ (GST) amorphization performed by quenching the 1073-K liquid to room temperature at different quench rates. (a) Total energy per atom of the 108-atom supercell as a function of quench time for quench rates $\Delta T/\Delta t = -0.45$, -2, -5, and -16 K/ps. Black lines show interpolation of the data to highlight trends. (b) Evolution of the number of square rings during the quench. (c)–(f) Final atomic structures generated by the quenching at -0.45, -2, -5, and -16 K/ps, respectively. A completely crystalized structure is shown in (c), an amorphous structure with an embedded crystalline cluster in (d), an amorphous structure with a high density of square rings in (e), and an amorphous structure with a low density of square rings in (f). Ge, Sb, and Te atoms are colored ochre, yellow, and cyan, respectively.

exhibits several planar structures containing multiple square rings. We note that the experimentally measured electrical resistance is very sensitive to the structural state (degree of crystallinity).

The crystallization of GST can occur over a wide range of temperature. To evaluate the effect of annealing temperature on the crystallization rate, we annealed the three amorphous samples [quenched at -2 in Fig. 1(d), -5 in Fig. 1(e), and -16 K/ps in Fig. 1(f)] at four temperatures, 500, 600, 700, and 800 K. No thermal annealing was performed on the structure shown in Fig. 1(c), since it was fully crystallized. Figures 2–4 show the results of these thermal annealing studies.

Figure 2 shows the results of annealing the amorphous sample formed by quenching at the highest rate, -16 K/ps [Fig. 1(f)]. The results indicate that annealing at different temperatures leads to different crystallization scenarios. Upon annealing at 500 K, the energy shows a nearly monotonic decay over ~0.9 ns before a steady state is achieved [see the magenta curves in Figs. 2(a) and 2(b)]. This suggests that a crystal nucleus/cluster forms rapidly and then grows to encompass the entire sample on this time scale. At higher annealing temperatures (600 and 700 K), a crystalline cluster forms and grows within a few hundred picoseconds. Interestingly, during a 700-K anneal, the energy initially increases before dropping smoothly, as we observed in the 500-K anneal [see the green curve in Fig. 2(a)]. This indicates that the order in the system initially decreases before a stable nucleus is formed and grows. The initial increase in the energy seems to be the result of the dynamic formation and disappearance of subcritical nuclei. These fluctuations are also seen in the ring statistics [Fig. 2(b)] during an early stage of the 700-K anneal. Note that black lines in Fig. 2(a) are averages over a 1-ps time window to reduce fluctuations. Curves in Fig. 2(b) are averages in a 0.9-ps time window as well. The vertical colored dashed lines in Figs. 2(a) and 2(b) indicate the estimated onset and end times of crystallization at different annealing temperatures.

Figures 2(c)–2(e) show the atomic structures at the end of the 1.5-ns annealing at 500, 600, and 700 K. In all cases, we see crystalline, but defected, GST. On the other hand, annealing at 800 K leads to a much different scenario. In this case, no crystallization is observed by examining the atomic structure [Fig. 2(f)], energy [Fig. 2(a)], or ring statistics [Fig. 2(b)]. It is interesting to note that 800 K was too low to induce crystallization of the high-temperature liquid at the slowest cooling rate [see Fig. 1(a)]. Because the square ring statistics data were averaged over 50-ps windows to reduce the magnitude of the fluctuations, the curves in Fig. 2(b) do not start at exactly the same value (as would be expected without the use of such a window).

The differences among the curves shown in Figs. 2(a) and 2(b) are due to both differences in structure and different temperatures. To account for the temperature effect we relaxed the initial and final structures and calculated both the energy and number of square rings (the results are shown in Table I). The initial energy per atom is -3.633 eV and the initial number of square rings is 69 following the quench to 0 K. After annealing at 500, 600, 700, and 800 K and quenching again to 0 K, the energy and number of rings are -3.695, -3.694, -3.700, and -3.594 eV, and 178, 189, 194, and 58 rings, respectively. This demonstrates that the degree of crystal

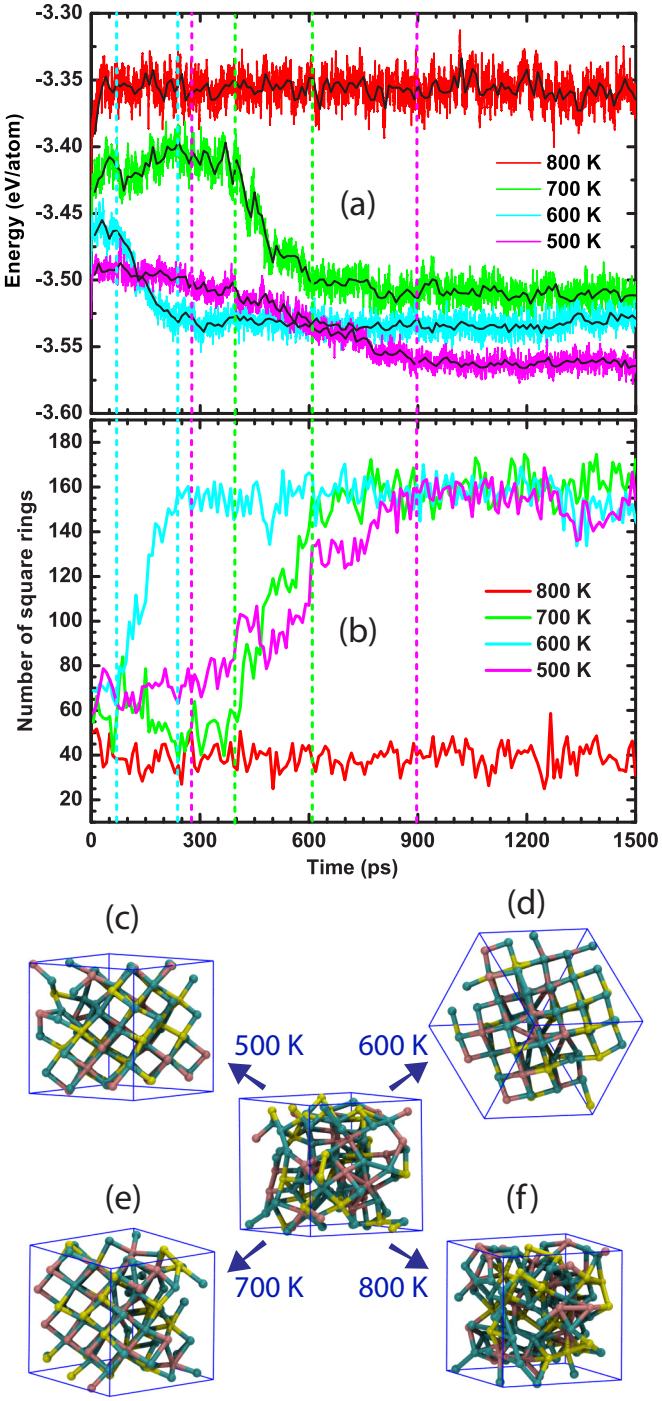

FIG. 2. Annealing of the amorphous structure generated by quenching at $\Delta T/\Delta t = -16\,\mathrm{K/ps}$ [Fig. 1(f)]. (a) Total energy per atom as a function of annealing time for 500-, 600-, 700-, and 800-K anneals. (b) Evolution of the number of square rings during annealing. (c)–(f) Final structures generated after annealing for 1.5 ns at 500, 600, 700, and 800 K. Colored dashed lines in (a) and (b) indicate the onset and end of the crystallization process for temperatures 500, 600, and 700 K. No crystallization is observed at 800 K.

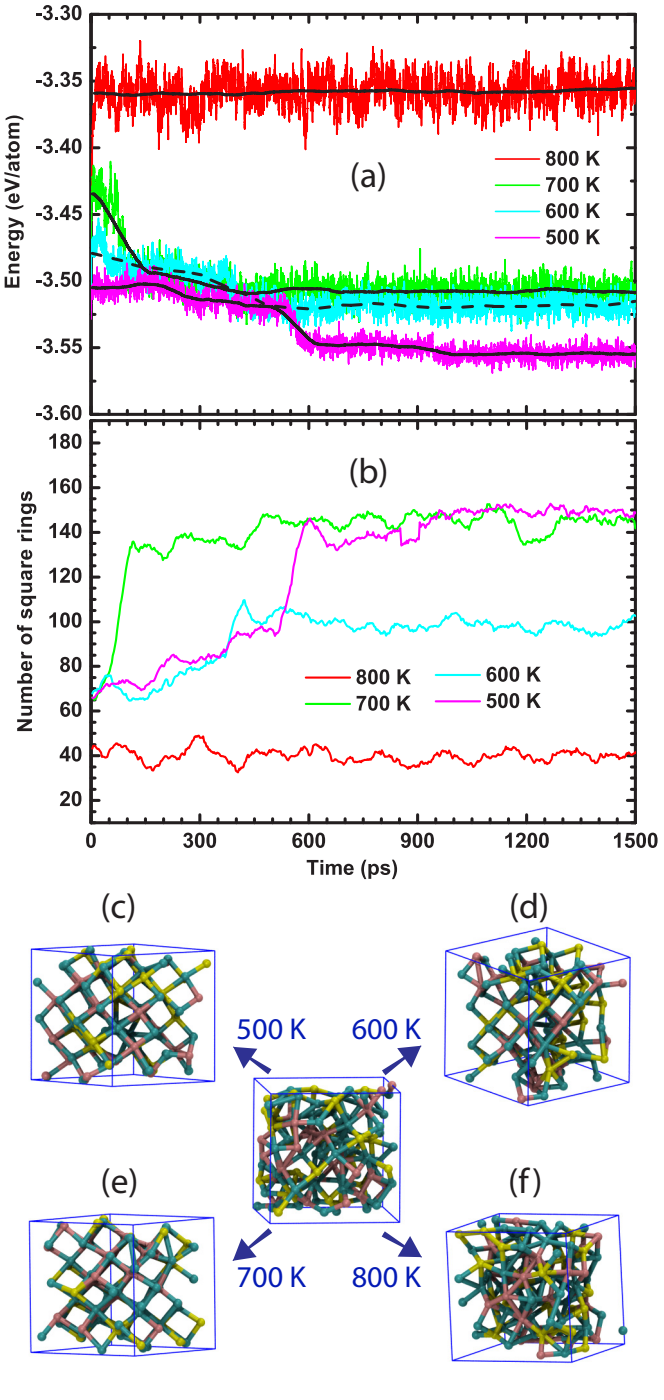

FIG. 3. Annealing of the amorphous structure with a high density of square rings generated with $\Delta T/\Delta t = -5\,\mathrm{K/ps}$, as shown in Fig. 1(d). (a) Total energy per atom as a function of annealing time for annealing temperatures 500, 600, 700, and 800 K. (b) Evolution of the number of square rings during annealing. Fluctuation in (b) is reduced averaging data points over a 50-ps window. (c)–(f) Final structures generated after 1.5-ns annealing at 500, 600, 700, and 800 K. As shown in the structures (c)–(e) the models annealed at 500–700 K crystallize while (f) shows that annealing at 800 K shows no signs of crystallization. Atoms colors in (c)–(f) follow the same pattern as in Fig. 1.

perfection, after correcting for thermal fluctuations, is indeed sensitive to annealing temperature.

Figure 3 shows the results of annealing of samples prepared by quenching at -5 K/ps (see Fig. 1). As discussed above, this sample has a higher number of square rings than the liquid structure or that obtained at a higher quench rate; these

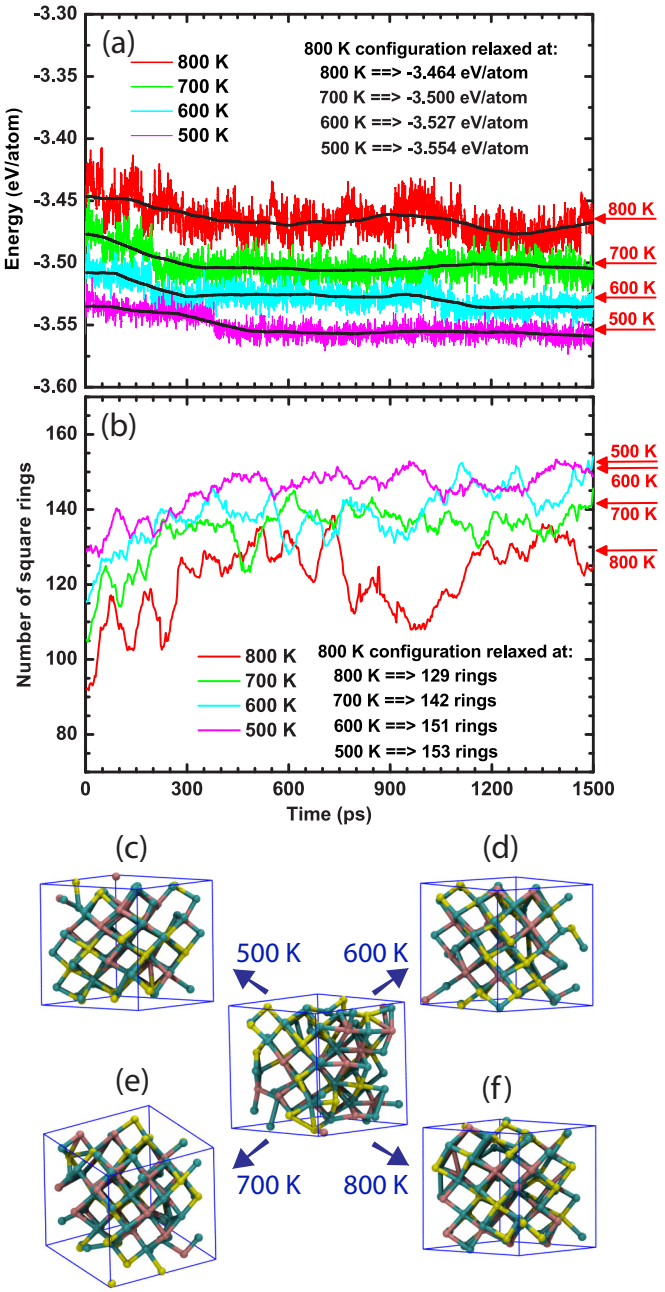

FIG. 4. Annealing the structure formed via a quench at $\Delta T/\Delta t = -2\,\mathrm{K/ps}$. Note this structure has a clearly discernible initial crystalline cluster—see Fig. 1(c). (a) Total energy per atom as a function of simulation time for annealing at 500, 600, 700, and 800 K. (b) Evolution of the number of square rings during annealing. (c)–(f) Structures observed following the 1.5-ns anneal at 500, 600, 700, and 800 K. The effect of temperature on the energy and number of square rings is highlighted by taking the structure from 800 K after the 1.5-ns anneal and holding it at different temperatures for 15 ps, as indicated by the arrows on the right in (a) and (b).

square rings may serve as seeds for crystal growth (crystal templates). Earlier work suggests that their presence facilitates crystallization [14]. These crystal seeds promote the swift generation of crystalline clusters in the temperature range 500–700 K. This contrasts with the simulation data shown in Fig. 2, where crystal nucleus generation depends on the annealing temperature. However, the absence of crystallization of the sample prepared by quenching at −5 K/ps upon annealing at 800 K for 1.5 ns is consistent with that observed in the fast quenched (−16 K/ps) sample (Fig. 2). This suggests that the formation of a crystal nucleus at 800 K requires times longer than the current 1.5-ns anneal. The annealed structures following the entire 1.5-ns anneals are illustrated in Figs. 3(c)–3(f). Note that the sample annealed at 600 K shows incomplete crystallization. This is counterintuitive and appears inconsistent with the rest of the results. We suspect that this is a stochastic effect and if the simulations were performed several times, the preponderance of results would indicate full crystallization under these conditions (only one simulation was prepared for each set of annealing conditions because of computational cost). As for the data in Figs. 2(a) and 2(b), we relaxed the initial and final structures to assess the effect of temperature and to compare the actual differences in the quenched and annealed structures (see Table I). At $T = 0\,\mathrm{K}$, the initial energy per atom is −3.639 eV and the initial number of square rings is 83. Upon annealing at 500, 600, 700, and 800 K, the relaxed energy and number of rings reach the values of −3.687, −3.682, −3.698, and −3.588 eV, and 174, 125, 170, and 44 rings, respectively. This again demonstrates that the main effect of annealing at different temperatures is structural, rather than caused by thermal fluctuations.

Thermally annealing the amorphous structure produced by quenching at −2 K/ps (see Fig. 4) contrasts sharply with the effects of annealing the structures formed at the higher quench rates (Figs. 2 and 3). Recall that the sample formed at this quench rate had a large crystalline structure embedded in the amorphous structure [see Fig. 1(d)]. The annealing behavior of this sample is illustrated in Fig. 4. Unlike for the sample prepared at higher quench rates prior to annealing (see Figs. 2 and 3), here no abrupt drop in energy occurs. Rather, the energy [Fig. 4(a)] declines slowly and the number of square rings [Fig. 4(b)] increases slowly with time at all annealing temperatures; both quantities approach a time-independent yet temperature-dependent steady state. The resulting crystal structures after a 1.5-ns annealing time are illustrated in Figs. 4(c)–4(f). Unlike for more quickly quenched structures, here, the 800-K annealing does lead to crystallization. This is presumably because in this case, the crystalline seed formed during the slow quenching was of a sufficient size to grow quickly at this temperature. The thermodynamic driving force for crystallization at 800 K, albeit small compared with lower temperatures, was sufficient to make this exceptionally large crystalline seed/nucleus supercritical. In other words, for the large crystalline seed present, there is no energetic barrier for further growth. This alludes to the predictions of the classical nucleation and growth theory [35–39].

One should note two peculiar features associated with annealing the amorphous sample formed at a quench rate of −2 K/ps. First, the initial energy values for every curve in Fig. 4(a) are noticeably lower than those for the samples prepared at higher quench rates [see Figs. 2(a) and 3(a)]. This is a clear result of the presence of a high fraction of crystalline material in the amorphous sample generated at −2 K/ps; the initial high number of square rings makes this observation quantitative. Second, all of the crystallized

TABLE I. Energies and number of square rings for the quenched and annealed structures relaxed to $T = 0$ K. The first column indicates the rate at which the initial structure was quenched. Annealing temperature indicates the temperature that the quenched structured was annealed for 1.5 ns.

Quench rate (K/ps)	Annealing temperature (K)	Energy (eV/atom)	Number of square rings
16	Quenched structure	−3.633	69
16	500	−3.695	178
16	600	−3.694	189
16	700	−3.700	194
16	800	−3.594	58
5	Quenched structure	−3.640	83
5	500	−3.688	174
5	600	−3.682	125
5	700	−3.698	170
5	800	−3.588	44
2	Quenched structure	−3.664	144
2	500	−3.689	165
2	600	−3.693	193
2	700	−3.695	182
2	800	−3.683	178
0.45	Quenched structure	−3.681	161

samples [see Figs. 4(c)–4(f)] have visibly fewer structural defects (e.g., such as "wrong" bonds). Since, in this case, the crystal nucleus is already supercritical at all of the annealing temperatures examined, crystal growth occurs from a single, nearly ideal crystallite. Since the crystallization process occurs quickly in this case, most of the 1.5-ns anneal simply perfects the structure, annealing out structural defects. As a side note, it should be emphasized that while crystallization is complete at all annealing temperatures, the number of square rings does not converge to the same value due to the effects of temperature on the ring statistics.

A comment should be made here on the choice of the relatively narrow range of quench rates used in this study. The range of quench rates from −0.45 to −16 K/ps spans less than two orders of magnitude. Nonetheless, the results show that those are the relevant quench rates for GST, since within this range of quench rates the quench process generates well contrasting amorphous structures. Similar quench rates have been used in previous simulations of GST [6,11]. Experimentally, while it is challenging to estimate accurately the quench rates in PCM devices, it has been demonstrated that small confined device cells can be amorphized by electric pulses within 400 ps [40]. That corresponds to a quench rate of ∼2 K/ps, right within the range chosen here.

The results presented above show the interaction between the quench rate and annealing temperature on the crystallization rate of GST. Crystallization readily occurs in GST at temperatures in the 500–700 K range, but not at 800 K (or presumably above), except for the special case where a crystal seed is already present (i.e., when the amorphous state is in fact partially crystalline). To understand this behavior, we turn to the classical nucleation and growth theory [35–39]. A detailed discussion of the nucleation and growth process is out of the scope of this paper. Nonetheless, some relevant points must be highlighted to enable one to understand the reported results. One should note, however, that the theory in general applies to an ensemble of transforming volumes with multiple grains nucleating, growing, and interacting, i.e., by impingement and adherence [38]. Here, our discussion is limited and aimed at highlighting the essential aspects of the theory, which are valid even for such small systems as the one considered in this paper. Following the theory, the first step in the crystallization process is the generation of a stable crystal nucleus. When that occurs, the crystallization proceeds by a steady growth of the nucleus until the system is fully crystallized. For any specific amorphous structure, several factors affect the nucleation and growth process, such as temperature and pressure. Temperature affects both the driving force for crystallization and the crystal growth rate. The temperature was shown to have a large effect also on the kinetic prefactor in the crystallization of largely immobile systems such as the amorphous GST here [41]. The driving force for crystallization decreases (approximately) linearly with increasing temperature (the critical nucleus size is inversely proportional to the driving force), i.e., it is larger at 500 K than at 800 K, as alluded to above. This explains why crystallization does not occur during the anneals at 800 K while it does at lower temperatures, despite the fact that the crystalline state has a (slightly) lower free energy than the amorphous structure at 800 K. On the other hand, atomic diffusivities increase "Arrheniusly" with temperature. The diffusivities of Ge, Sb, and Te in the amorphous GST sample prepared by quenching at −16 K/ps are shown in Fig. 5 as a function of temperature.

The diffusivities are determined by measuring the rms displacements of each element over a period of 150 ps. This time is sufficiently large to have an accurate measurement and sufficiently short to minimize the effect of structural relaxation of the amorphous structure, which is, although, not completely absent. In the fastest crystallization case, as can be seen by the energy and number of square rings (cyan lines) for 600 K in Fig. 2, complete crystallization occurs at ∼300 ps. Therefore, alpha structural changes may occur in a short time, which is the reason we limited the rms displacements to 150 ps. Alpha/beta relaxations are primary/secondary relaxations occurring in

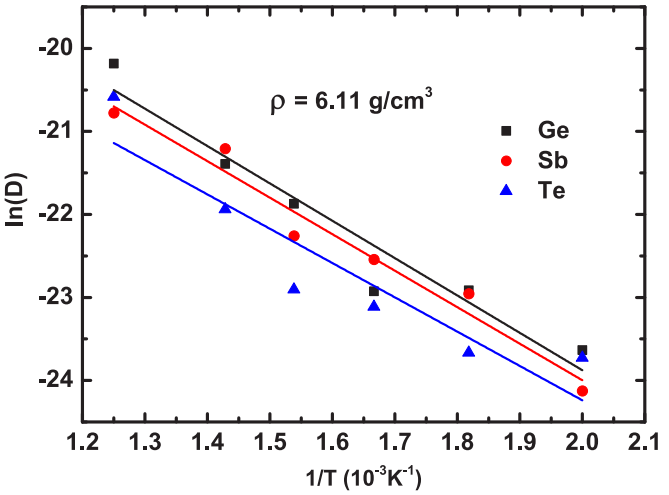

FIG. 5. Atomic diffusivities of GST. Atomic diffusivity (D) as a function of temperature in Arrhenius coordinates for the model amorphous structure (produced by a −16 K/ps quench) with a density 6.11 g/cm^3 (D is in units of 10^{-9} m^2/s).

glasses, e.g., as discussed in the review by Yu *et al.* [42]. The alpha relaxation is the relaxation responsible for the formation of the glass state while the beta relaxation is the one still active below T_g.

The activation energy for diffusion of all three elements in the amorphous GST sample is ∼0.5 eV, within the statistics of these computationally expensive calculations (see Fig. 5). The values of the activation energy are based on the diffusions calculated from a single simulation run. Because of this lack of statistical data, no error analysis over the value of the activation energy is predicted and no corresponding error bars are provided. The growth rate of GST crystals from a disordered phase depends linearly on the atomic diffusivities. The Arrhenius dependence of the diffusivities on temperature explains why crystal growth is faster at 600 and 700 K than at 500 K, despite the fact that the driving force for crystallization is larger at 500 K. That can be seen explicitly by the larger (negative slope) in the energy versus time plots at the higher temperatures [see Fig. 2(a)]. These two effects compete.

Both the nucleation and growth rates are affected by this competition, which gives rise to the observed *nose* in the CCT-TTT diagram [43]. This behavior is consistent with our simulation results. Note that we expect some variance associated with the restricted simulation statistics here. In particular, the nucleation time is a stochastic process that requires proper statistics to delineate a range of expected values. Therefore, the data obtained in this paper, while consistent with experimental data and in agreement with other simulation work, only provide an estimation of the crystallization kinetics of GST. Based on the energy versus time curves shown in Figs. 2(a) and 2(b), we estimated the onset and end times for crystallization. The data points are highlighted by colored dashed lines at 276.5 and 898 ps for 500 K, 70 and 240 ps for 600 K, and 387.5 and 605 ps for 700 K, respectively. The data are shown in Fig. 6(a) as open symbols and delineate the TTT diagram for GST. Since to be able to draw the TTT diagram both nucleation and growth processes should be present, only the data from the isothermal

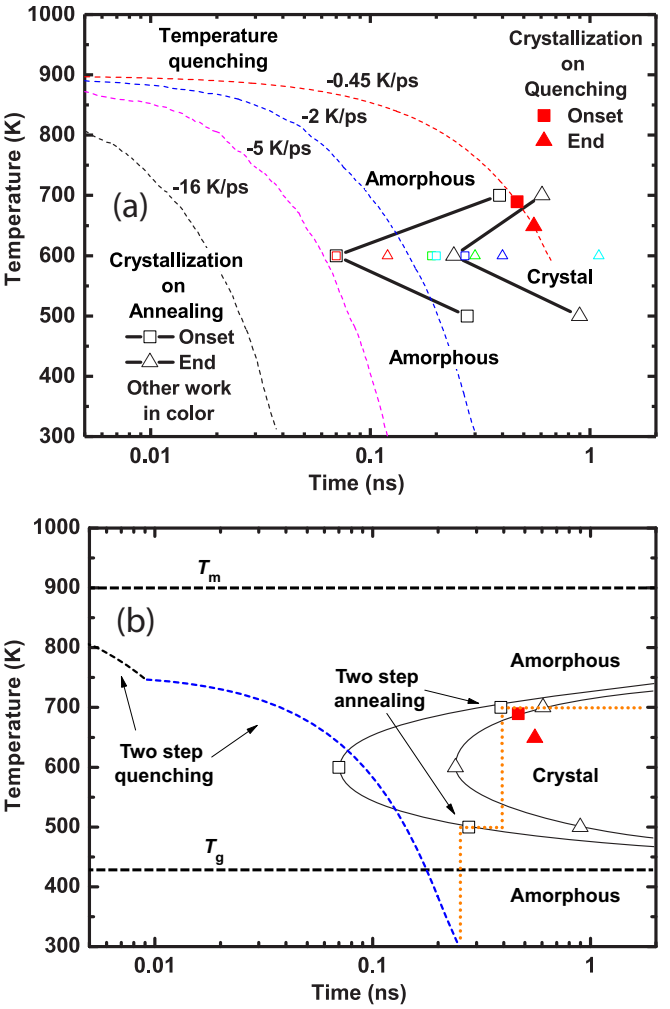

FIG. 6. GST combined continuous-cooling-transformation (CCT) and time-temperature-transformation (TTT) diagrams and possible optimized routes for the reversible switching cycle. (a) CCT-TTT diagram with data points based on estimated onset and end times for crystallization at the quench rate of −0.45 K/ps, shown as solid symbols, and at different annealing temperatures, shown as open symbols. Dashed black, magenta, blue, and red curves indicate different quench rates. (b) Possible routes to accelerate the amorphization, tailor the amorphous phase, and accelerate the crystallization by using multiple quenching rates and annealing temperatures. Solid curves illustrate the TTT diagram based on the data points shown in (a). The horizontal dashed black lines labeled T_m and T_g indicate the melting temperature 900 K, and the glass transition temperature 428 K, respectively.

annealing simulations of the amorphous generated with the quench rate −16 K/ps are utilized. The quenching curves are also indicated in Fig. 6(a), turning it into a combined CCT-TTT diagram. The onset and end times of the crystallization occurring during the quenching at −0.45 K/ps are indicated by the red solid symbols in Fig. 6(a). Since only one simulation is performed in each case we include data from the literature on simulations of similar systems to provide an idea about the range of values expected for the crystallization onset and end times. The data are shown as colored open symbols in Fig. 6(a). Data in red are from Lee and Elliot [16] (70–120 ps),

in green and purple from Lee and Elliot [14] (190–300 ps, and 270–400 ps), and finally in light blue from Kalikka *et al.* [23] (200–1100 ps). While the data ranges are comparable, one should consider that the system sizes and model preparation procedures in those works and the ones here are different and that may also affect the resulting crystallization times beyond the expected stochastic fluctuation on the values.

The nose of the CCT-TTT diagram is of critical importance. It indicates the minimum time for incubation and the ideal temperature for crystallization. One can see from the data that the nose of the CCT-TTT diagram is located at 600 K and 70 ps. Similar incubation times at 600 K are reported in the literature from AIMD simulations with different sizes and amorphous preparations [14,44]. From the nose of the CCT-TTT diagram one can calculate the critical cooling rate for amorphization. Considering cooling from the melting temperature (900 K), the critical cooling rate is −4.5 K/ps. This rate is consistent with our results, which indicate partial and full crystallizations at the quench rates −2 and −0.45 K/ps, respectively. The nose of the CCT-TTT diagram located at 600 K indicates the optimal temperature, within those considered here, for crystallization. The importance of the CCT-TTT diagram of GST was highlighted previously [2,45,46]. Unfortunately, due to the extremely fast reversible transformation and the ultrafast heating and cooling rates associated with the required experiments, a CCT-TTT diagram of GST has yet to be reported.

The formation and growth of crystal clusters may also be affected by the simulation size (the AIMD simulations were performed with only ∼100 atoms). In order to test this, simulations were also performed on a 63-atom model system (the results presented above had 108 atoms). Results are presented in the Supplemental Material (SM) [47]. As expected, the 63-atom model crystallizes more easily that the 108-atom model. The model crystallizes quickly under annealing at all temperatures considered in this paper, including the temperature where no crystallization is observed in the 108-atom GST model (800 K) (please see Fig. S1 in the SM). In contrast, the results discussed here for the 108-atom model agree well with those of a larger (207-atom system). As shown in Fig. S2, crystallization follows the predictions discussed for the 108-atom system. The exception is the annealing at 700 K, which shows no crystallization during the 1.4-ns annealing time performed. These results suggest that the predictions presented above are not unduly affected by simulation model size. The additional simulation results for crystallization of the 63- and 207-atom systems are discussed in the SM. It should be noted that size effects are inherent in the performance of PCM cells. For example, it was reported that GST PCM cells display a strong size-dependent reduction in switching speed from ∼70 to below ∼10 ns, reducing the cell size from 300 to 50 nm [6]. Another report demonstrated that reset/set operations of GST PCM cells of 19-nm size are reduced to 400 ps/2.5 ns [40]. It is clear that with the reduction of device dimensions, size effects play increasingly important roles in enabling ultrafast reversible cycles. On the basis of these reports, our results highlight the amorphization/crystallization kinetics of very small systems which set the limit expected for the performance of such PCM devices.

Nucleation and growth can also be affected by pressure. The evaluation of the pressure effect on the crystallization

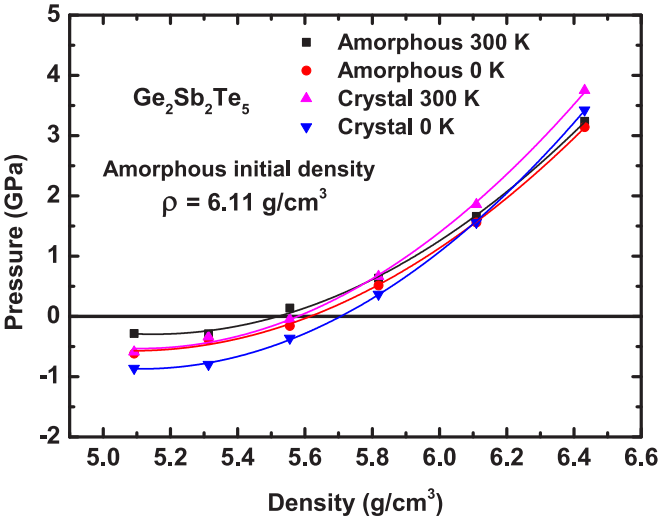

FIG. 7. The equation of state of GST. Pressure as a function of density for amorphized and crystallized GST at $T = 300$ and 0 K.

is a topic that exceeds the scope of this paper and is left to be presented in a future publication. In this paper, we focused on the reversible cycle in confined cells, which are expected to display nearly constant density, justifying our choice of simulations with fixed system size. Therefore, the results presented above were all obtained from simulations performed at a fixed density of 6.11 g/cm^3. This density was chosen as a compromise between the experimental density values of amorphous and crystal GST and was the density adopted in previous simulations of GST cycling [11]. The use of fixed volume (density) simulations implies that the sample will lack density changes and suggests that the amorphization and crystallization processes will occur at nonzero pressure. In order to evaluate the effects of this stress, we performed a series of simulations of the amorphous and crystalline phases at different densities. The amorphous model was that generated at the quench rate −16 K/ps. At a density of 6.11 g/cm^3, this sample was under a hydrostatic pressure of 1.66 GPa at 300 K and 1.56 GPa at 0 K, and the density dependence of the pressure is reported in Fig. 7. The pressure-density relation was also evaluated for the crystallized structure found by annealing this amorphous structure at 700 K (this was the best-crystallized structure/had the most square rings—see Table I and Fig. 2). Surprisingly, at $T = 300$ K, the equilibrium pressure of the crystallized model is 1.86 GPa, similar to that of the amorphous model. This is somewhat surprising since it is expected that the zero-pressure crystalline GST will have a lower density than its amorphous counterpart. We note that the crystalline model examined is not a perfect crystal, as an inspection of Fig. 2(e) demonstrates. Perhaps the incomplete crystallization is a result of the density constraint. We note that the development of stress/pressure is thought to be unavoidable during reversible switching of GST in both films and PCM devices due to geometric constraints. In a thin-film geometry, the stress developed through amorphization/crystallization cycling will be a plane stress [48]. In contrast, the crystallization of GST in highly confined cells in PCM devices is expected to be closer to the hydrostatic pressure, given the low compliance of the

confinement cells [49,50]. Taking these cases in consideration, the results discussed here are most relevant for the reversible cycle occurring in GST in confined PCM cells. Since there is relatively little difference between the energy of the defected crystalline material and the amorphous material, we should expect that the constraint provided by the low-compliance cells in a PCM device will have little effect on the amorphization/crystallization thermodynamics.

The results presented here provide insights into how GST crystallization rates depend on the quench rate and annealing temperature. Considering that the time required for crystallization is typically one order of magnitude larger than the amorphization time in experiments [51], the reversible switching time is determined largely by the crystallization rate. Therefore, changing crystallization rates allow for the optimization of the switching cycle. In PCM devices, both quench rates and annealing temperatures can be controlled accurately by choosing the applied current pulse amplitudes. Therefore, the results presented here provide important insights into the tuning of the PCMs to obtain optimal device speeds.

The idea of fine tuning the reversible switching by tweaking the amorphization process to produce suitable amorphous structures was initially proposed by Suh *et al.* [24]. In that work, the authors programmed the voltage pulse shape to generate different quench and annealing rates (reset and set operations) in a 90-nm-thick GST film. Even though their report was purely experimental and neither the actual quench rates nor the level of crystallinity were evaluated directly, the proposed idea is very similar to the one here. Different cooling rates generate different amorphous structures, each with a unique crystallization rate. Suh *et al.* also showed that for a given reset structure, the set pulse amplitude had a direct effect on the observed time delay for switching. This is in line with our results that show that different annealing temperatures lead to different crystallization rates.

The results presented here demonstrated that crystallization time depends on both the quench rate and annealing temperatures; this suggests that these two process parameters should be optimized together to maximize the crystallization rate. One may envision that by combining two quenching rates during the amorphization process, e.g. -16 and -2 K/ps, a suitable amorphous structure with a preformed crystal nucleus will be generated in a shorter amorphization time than by simply using a -2 K/ps quench rate. Such a strategy of combining the application of multiple electric pulses to tailor amorphous states was recently attempted [52]. Similarly, by combining two annealing temperatures, e.g., 500 and 700 K, one could optimize both the nucleation time and growth time, significantly shortening the overall crystallization rate. Such a combination of multiple quench rates or annealing temperatures is shown in the illustration of the TTT diagram on Fig. 6(b). The melting (900 K) [46] and glass transition (428 K) [53] temperatures are indicated and delineate the CCT-TTT diagram limits. While the combination of multiple quench rates or multiple annealing temperatures is an attractive idea to optimize the reversible cycle in GST, the simulation data suggest that the largest effect may come from the use of the former. The data in Figs. 6(a) and 6(b) indicate that the incubation time is shorter at 600 K (70 ps). They also indicate that the total crystallization time from the nucleation point is similar at 600 K (178 ps) and 700 K (220 ps). Therefore, the data indicate that both incubation time and crystal growth occur optimally at 600 K. In contrast, if a nucleus is already nucleated in the amorphous, by using multiple quench rates, then crystallization should occur promptly, as it is indicated by the data in Figs. 3 and 4. An additional and desirable consequence of accelerating the reversible switching in PCM devices is that the whole process will be more energy efficient. This is a key factor in the development of and competition between different electronic device technologies, including memories [54].

It should be noted that in actual PCM devices, the complete cycle involves truly amorphous and crystalline states at room temperature. In the complete cycle, it has been demonstrated experimentally and in simulations that the actual state of the amorphous structure has an effect on the speed of the PCM device. For example, Loke *et al.* [6] applied a constant low voltage pulse to the PCM device to induce a prestructural ordering (incubation) which was subsequently demonstrated to speed up the crystallization process to 500 ps. In contrast, in our paper, we propose to use different quench rates to generate a suitable amorphous structure that could be used directly to speed up the crystallization without the utilization of a preliminary low voltage pulse.

IV. CONCLUSIONS

In summary, nanosecond AIMD simulations were employed to investigate the complex processes of amorphization and crystallization of $Ge_2Sb_2Te_5$ (GST) and to characterize the effect of the quenching rate and annealing temperature on these processes. The simulations showed a strong effect of the quenching rate on the structure of the amorphous phase. Amorphous structures with relatively low densities of crystal seeds (square rings) were generated at a quench rate of -16 K/ps, while the structure completely crystallized at a quench rate of -0.45 K/ps; the density of crystal-like structural features increased with decreasing quench rates. A strong effect of annealing temperatures, in the range 500–800 K, was also found during the crystallization of the amorphous structures. These results can be understood in terms of classical nucleation and growth considerations. Annealing at 500 K resulted in a relatively short incubation time, but a low growth rate. In contrast, annealing at 800 K resulted in slow crystal nucleation. At this annealing temperature, crystallization is not observed at all, with the exception of an amorphous structure with a relatively large preexisting crystalline cluster (i.e., the amorphous structure formed at a quench rate of -2 K/ps). The data are used to draw a combined continuous-cooling-transformation (CCT) and time-temperature-transformation (TTT) which suggests that the optimal temperature for crystallization is 600 K. Overall, the results indicate that the processes of amorphization and crystallization may be conveniently tuned by an optimal choice of both the quench rate and annealing temperature. Alternatively, multiple quench rates and annealing temperatures could be used to further optimize the reversible cycle. The simulation data in particular indicate that a combination of multiple quench rates is the most promising approach to optimize the reversible cycle and enhance the device switching rates.

ACKNOWLEDGMENTS

This work was supported in part by the A*STAR Computational Resource Centre through the use of its high-performance computing facilities. The authors thank Dr. Song Wendong for discussions and advice.

[1] M. H. R. Lankhorst, B. W. S. M. M. Ketelaars, and R. A. M. Wolters, Nat. Mater. **4**, 347 (2005).
[2] M. Wuttig and N. Yamada, Nat. Mater. **6**, 824 (2007).
[3] V. L. Deringer, R. Dronskowski, and M. Wuttig, Adv. Funct. Mater. **25**, 6343 (2015).
[4] W. Welnic and M. Wuttig, Mater. Today **11**, 20 (2008).
[5] G. W. Burr, M. J. Breitwisch, M. Franceschini, D. Garetto, K. Gopalakrishnan, B. Jackson, B. Kurdi, C. Lam, L. A. Lastras, A. Padilla, B. Rajendran, S. Raoux, and R. S. Shenoy, J. Vac. Sci. Technol. B **28**, 223 (2010).
[6] D. Loke, T. H. Lee, W. J. Wang, L. P. Shi, R. Zhao, Y. C. Yeo, T. C. Chong, and S. R. Elliott, Science **336**, 1566 (2012).
[7] T. Matsunaga, N. Yamada, and Y. Kubota, Acta Crystallogr., Sect. B **60**, 685 (2004).
[8] Z. Sun, J. Zhou, and R. Ahuja, Phys. Rev. Lett. **96**, 055507 (2006).
[9] J. L. F. Da Silva, A. Walsh, and H. Lee, Phys. Rev. B **78**, 224111 (2008).
[10] M. Krbal, A. V. Kolobov, P. Fons, J. Tominaga, S. R. Elliott, J. Hegedus, and T. Uruga, Phys. Rev. B **83**, 054203 (2011).
[11] J. Hegedüs and S. R. Elliott, Nat. Mater. **7**, 399 (2008).
[12] J. Hegedus and S. R. Elliott, J. Optoelectron. Adv. Mater. **11**, 1060 (2009).
[13] J. Hegedus and S. R. Elliott, Phys. Status Solidi **207**, 510 (2010).
[14] T. H. Lee and S. R. Elliott, Phys. Rev. Lett. **107**, 145702 (2011).
[15] T. H. Lee and S. R. Elliott, Phys. Rev. B **84**, 094124 (2011).
[16] T. H. Lee and S. R. Elliott, Phys. Status Solidi **249**, 1886 (2012).
[17] J. Kalikka, J. Akola, J. Larrucea, and R. O. Jones, Phys. Rev. B **86**, 144113 (2012).
[18] B. Prasai, M. E. Kordesch, D. A. Drabold, and G. Chen, Phys. Status Solidi **250**, 1785 (2013).
[19] B. Prasai, G. Chen, and D. A. Drabold, Appl. Phys. Lett. **102**, 041907 (2013).
[20] J. Liu, X. Xu, L. Brush, and M. P. Anantram, J. Appl. Phys. **115**, 023513 (2014).
[21] J. M. Skelton, D. Loke, T. H. Lee, and S. R. Elliott, Phys. Status Solidi **250**, 968 (2013).
[22] I. Ronneberger, W. Zhang, H. Eshet, and R. Mazzarello, Adv. Funct. Mater. **25**, 6407 (2015).
[23] J. Kalikka, J. Akola, and R. O. Jones, Phys. Rev. B **90**, 184109 (2014).
[24] D. S. Suh, K. H. P. Kim, J.-S. Noh, W.-C. Shin, Y.-S. Kang, C. Kim, Y. Khang, and I. K. Yoo, in *2006 International Electron Devices Meeting, San Francisco, CA* (IEEE, Piscataway, NJ, 2006), pp. 1–4.
[25] R. Hafner, J. Comput. Chem. **29**, 2044 (2008).
[26] J. P. Perdew, K. Burke, and M. Ernzerhof, Phys. Rev. Lett. **77**, 3865 (1996).
[27] M. Methfessel and A. T. Paxton, Phys. Rev. B **40**, 3616 (1989).
[28] P. E. Blöchl, Phys. Rev. B **50**, 17953 (1994).
[29] S. Kohara, K. Kato, S. Kimura, H. Tanaka, T. Usuki, K. Suzuya, H. Tanaka, Y. Moritomo, T. Matsunaga, N. Yamada, Y. Tanaka, H. Suematsu, and M. Takata, Appl. Phys. Lett. **89**, 201910 (2006).
[30] G. A. Tribello, F. Giberti, G. C. Sosso, M. Salvalaglio, and M. Parrinello, J. Chem. Theory Comput. **13**, 1317 (2017).
[31] S. V. King, Nature (London) **213**, 1112 (1967).
[32] L. Guttman, J. Non-Cryst. Solids **116**, 145 (1990).
[33] C. Zhang, B. Bansal, P. S. Branicio, R. K. Kalia, A. Nakano, A. Sharma, and P. Vashishta, Comput. Phys. Commun. **175**, 339 (2006).
[34] S. Le Roux and P. Jund, Comput. Mater. Sci. **49**, 70 (2010).
[35] W. A. Johnson and R. F. Mehl, Trans. Am. Inst. Min., Metall. Pet. Eng. **135**, 416 (1939).
[36] M. Avrami, J. Chem. Phys. **7**, 1103 (1939).
[37] M. Avrami, J. Chem. Phys. **8**, 212 (1940).
[38] M. Avrami, J. Chem. Phys. **9**, 177 (1941).
[39] L. Heireche and M. Belhadji, J. Optoelectron. Adv. Mater. **11**, 1058 (2009).
[40] W. J. Wang, L. P. Shi, R. Zhao, K. G. Lim, H. K. Lee, T. C. Chong, and Y. H. Wu, Appl. Phys. Lett. **93**, 043121 (2008).
[41] G. C. Sosso, G. Miceli, S. Caravati, F. Giberti, J. Behler, and M. Bernasconi, J. Phys. Chem. Lett. **4**, 4241 (2013).
[42] H. Bin Yu, W. H. Wang, and K. Samwer, Mater. Today **16**, 183 (2013).
[43] D. A. Porter, K. E. Easterling, and M. Y. Sherif, *Phase Transformations in Metals and Alloys*, 3rd ed. (CRC Press, Boca Raton, FL, 2009).
[44] J. M. Skelton, T. H. Lee, and S. R. Elliott, Appl. Phys. Lett. **101**, 024106 (2012).
[45] F. R. Liu, N. Bai, J. J. Zhao, X. X. Han, W. P. Zhou, X. Lin, and N. X. Sun, Appl. Phys. Lett. **103**, 051905 (2013).
[46] G. W. Burr, P. Tchoulfian, T. Topuria, C. Nyffeler, K. Virwani, A. Padilla, R. M. Shelby, M. Eskandari, B. Jackson, and B.-S. Lee, J. Appl. Phys. **111**, 104308 (2012).
[47] See Supplemental Material at http://link.aps.org/supplemental/10.1103/PhysRevMaterials.2.043401 for additional information about AIMD simulation parameters and data for size scale effects on the crystallization kinetics.
[48] Q. Guo, M. Li, Y. Li, L. Shi, T. C. Chong, J. A. Kalb, and C. V. Thompson, Appl. Phys. Lett. **93**, 221907 (2008).
[49] M. Li, L. Shi, R. Zhao, T. C. Chong, and Y. Li, Jpn. J. Appl. Phys. **49**, 058003 (2010).
[50] T. P. L. Pedersen, J. Kalb, W. K. Njoroge, D. Wamwangi, M. Wuttig, and F. Spaepen, Appl. Phys. Lett. **79**, 3597 (2001).
[51] M. Terao, T. Morikawa, and T. Ohta, Jpn. J. Appl. Phys. **48**, 080001 (2009).
[52] T. H. Lee, D. Loke, K.-J. Huang, W.-J. Wang, and S. R. Elliott, Adv. Mater. **26**, 7493 (2014).
[53] S. Senkader and S. D. Wright, J. Appl. Phys. **95**, 504 (2004).
[54] P. Zhou, B. Zhao, J. Yang, and Y. Zhang, ACM SIGARCH Comput. Archit. News **37**, 14 (2009).